ASME Journal of Dynamic Systems, Measurement, and Control
Online journal at:
https://asmedigitalcollection.asme.org/dynamicsystems

Matteo Acquarone
Energy Science and Engineering,
Stanford University,
Stanford, CA 94305
e-mail: matteo.acquarone@polito.it

Gabriele Pozzato
Energy Science and Engineering,
Stanford University,
Stanford, CA 94305
e-mail: gpozzato@stanford.edu

Corey James
Department of Chemistry and Life Science,
United States Military Academy,
West Point, NY 10996
e-mail: corey.james@westpoint.edu

Simona Onori
Energy Science and Engineering,
Stanford University,
Stanford, CA 94305
e-mail: sonori@stanford.edu

Offline and Online Exergy-Based Strategies for Hybrid Electric Vehicles

Exergy-based control strategies for ground hybrid electric vehicles (HEVs) enable to pursue unconventional optimization goals that are inaccessible when standard energy-based modeling frameworks based on fuel consumption minimization are used. In this work, we formulate and solve offline and online exergy-based optimization strategies for military HEVs aimed at the minimization of genset exergy destruction and thermal emissions to increase vehicle efficiency and minimize the risk of thermal imaging detection, respectively. We refer to the offline version of these strategies as exergy minimization strategies (ExMSs). Adaptive ExMSs (A-ExMSs) are then formulated for online implementation. Moreover, charge increasing (CI) ExMSs and A-ExMSs are developed to charge the battery as much as possible during a driving mission that is followed by a silent watch phase. To assess the performance of the proposed strategies, the results obtained by the ExMSs and A-ExMSs are compared to the benchmark solutions obtained by Dynamic Programming.
[DOI: 10.1115/1.4066764]

1 Introduction

Exergy is defined as the maximum useful work that can be obtained from a thermodynamic system or process with respect to a given reference state [1]. Exergy analysis is a thermodynamic analysis technique routed in the first and second laws of thermodynamics [2] that provides new design and control opportunities over conventional energy-based approaches. First, exergy analysis enables to quantify the irreversibilities of a process, identify the sources of inefficiency, and assess the quality, rather than just the quantity, of energy transfers [3]. Exergy-based optimization can be pursued to minimize exergy destruction, a quantity that accounts for all the irreversibilities of a process, and is not quantifiable through energy-based methods.

Exergy analysis has been proposed for a variety of applications, such as the optimization and control of power plants [4], photovoltaic systems [5], and aerospace technologies [6]. For instance, several exergy-based control strategies have been studied in the context of energy conversion systems in buildings [7]. In Ref. [8], after assessing the exergy balance of a building, an exergy-based model predictive control is developed to minimize the exergy destruction of a heating, ventilation, and air conditioning system. In the context of ground vehicles' powertrains, exergy control strategies have been developed to enhance the performance of internal combustion engines (ICEs) [9]. In Ref. [10], the ICE exergetic efficiency is maximized by an optimal controller, achieving lower fuel consumption than the traditional energy-based combustion control. Moreover, a comprehensive exergy modeling framework for hybrid electric vehicles (HEVs) is developed in Ref. [11]. The vehicle exergetic balance is assessed through the quantification of exergy transfer and destruction for each component of the powertrain. The study shows that the battery exergy destruction and losses are, in practice, negligible when compared to the ones from the ICE, which in turn contributes to about 80% of the overall exergy losses of the vehicle, when the Worldwide Harmonized Light Vehicles Test Procedure driving cycle is used.

While the automotive market is shifting toward battery only electric vehicles adoption, military vehicles are moving toward hybridization [12]. The full electrification of military powertrains is not practical due to the high weight of the battery pack, the limited range [13], and the logistical challenges associated with charging a fully electric vehicle on the battlefield. Although HEVs have been traditionally controlled through energy-based management strategies to optimize the onboard energy flow [14], exergy-based approaches are particularly useful in military applications to pursue nonstandard optimization goals. For instance, the reduction of thermal imaging detection is a critical goal for military vehicles that cannot be achieved by standard energy management strategies. Moreover, unconventional requirements must be satisfied during some military operations by the control strategy. For instance, the battery needs to be charged as much as possible for those driving missions that are followed by a silent watch operation. During silent watch, the battery pack is the only active power source that provides the necessary power to all the auxiliary systems in the vehicle.

Two exergy-based management strategies for HEVs are proposed in Ref. [15], leveraging the exergetic modeling framework developed in Ref. [11]. In Ref. [15], the proposed strategies are solved offline through Dynamic Programming (DP). Hence, a gap remains in the realm of real-time deployable strategies. This paper seeks to address this gap by proposing a solution in the form of adaptive online strategies.

Contributed by the Dynamic Systems Division of ASME for publication in the Journal of Dynamic Systems, Measurement, and Control. Manuscript received October 24, 2023; final manuscript received September 19, 2024; published online November 4, 2024. Assoc. Editor: Marcello Canova.

Several online energy-based strategies for HEVs have been proposed in the literature, such as rule-based [16], model-predictive control [17], reinforcement learning algorithms [18], and equivalent consumption minimization strategy (ECMS) [19]. The ECMS aims to minimize the equivalent fuel consumption, defined as the sum of the actual fuel consumption and a virtual fuel consumption associated with battery usage. The battery virtual fuel consumption is weighted through an equivalence factor. The value of equivalence factor that guarantees charge sustainability, which is driving cycle dependent, corresponds to the optimal costate value in the Pontryagin's Minimum Principle formulation (PMP) of the energy management strategy [19]. For real-time operation, adaptive-ECMS (A-ECMS) strategies are developed to update the equivalence factor online using the feedback from the battery state of charge of the battery (SOC) [20].

In this paper, we utilize the exergy-based modeling framework introduced in Ref. [15] to develop offline and online (adaptive) exergy-based control strategies. We refer to these strategies as exergy minimization strategies (ExMS) and adaptive exergy minimization strategies (A-ExMS), respectively. The main contributions of this study are as follows:

(1) Formulation of two exergy-based control strategies for hybrid electric ground military vehicles in the form of exergy minimization strategies aimed at the minimization of genset exergy destruction ($\text{ExMS}_{\text{dest}}$) and thermal emissions ($\text{ExMS}_{\text{thermal}}$) to optimize the overall vehicle efficiency and minimize the risk of thermal imaging detection.
(2) Formulation of A-ExMSs for online implementation.
(3) Development of charge sustaining (CS) and charge increasing (CI) ExMSs to achieve different battery state of charge targets at the end of the mission. Specifically, a CI ExMS is designed to charge the battery for silent watch mission readiness. This is achieved with the formulation of a new penalty function in the optimization problem.
(4) Comparative analysis between ExMSs, A-ExMSs, and the benchmark solution from DP.

The remainder of the paper is organized as follows: In Sec. 2, the series HEV and its components are modeled and the exergy model of the genset system is presented. Section 3 formalizes the optimal control problems for the standard ECMS and the ExMSs in terms of exergy destruction and thermal emissions minimization. In Secs. 4 and 5, the charge sustaining and charge increasing ExMS and A-ExMS are formulated. Finally, the solutions obtained through the proposed strategies are shown and compared in Sec. 6, and conclusions are drawn in Sec. 7.

2 Hybrid Electric Vehicles Model

The model of the series military HEV considered in this study borrowed from Ref. [15] (and based on the previous works [21] and [22]) is shown in Fig. 1. The main powertrain components are: a 260 kW diesel ICE, a 268 kW electric induction generator, a 10.9 kWh lithium-ion battery pack, and four 95 kW Interior Permanent Magnet Synchronous in-hub Motors. The generator, the battery pack, and the electric traction motors are connected through the AC-DC and AC-AC converters [23]. In this work, we describe the exergetic models of the electric generator and the ICE, while we recall the energetic model of the electric motors, battery, generator, and ICE (details on the exergy models of these components can be found in Refs. [11,15]). In the remainder of the paper, when computing the exergetic terms, the reference state is defined by the environment pressure $P_0 = 1$ bar and temperature $T_0 = 25\,^{\circ}\text{C}$ [11].

2.1 Vehicle Longitudinal Dynamics. The energy balance along the vehicle longitudinal axis is used to obtain an expression for the power at the wheels $P_w = v(M\dot{v} + Mg\sin\theta + C_r Mg\cos\theta + \frac{1}{2}\rho_a A C_x v^2) + P_{\text{brake}}$, where v is the vehicle velocity, M is the vehicle mass, g is the acceleration due to gravity, P_{brake} is the mechanical brake power, C_r and C_x are the roll and drag coefficients, respectively, ρ_a is the air density, A is the frontal area of the vehicle, and θ is the road slope.

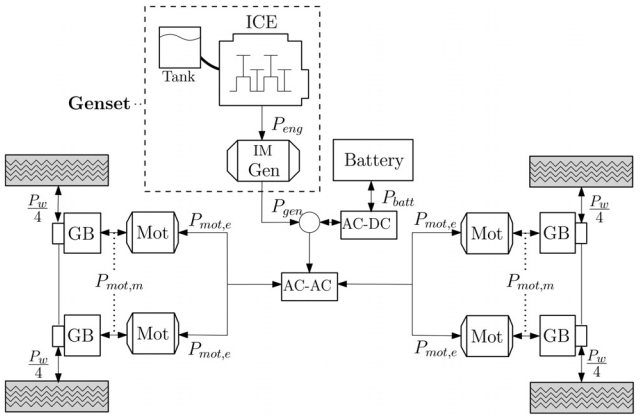

Fig. 1 Series HEV configuration [15]

2.2 Electric Traction Motors. The traction power is provided by four Interior Permanent Magnet Synchronous in-hub Motors. Each motor is characterized by the static efficiency map (shown in Ref. [11]), which is a function of motor speed ω_{mot} and torque τ_{mot}. The electric power $P_{\text{mot,e}}$ required by each individual electric motor is a function of motor efficiency η_{mot}, gearbox efficiency η_{GB}, and power requested at the wheels P_w

$$P_{\text{mot,e}} = \begin{cases} \dfrac{P_w}{4 \cdot \eta_{\text{GB}} \cdot \eta_{\text{mot}}}, & \text{if } P_w \geq 0 \\ \dfrac{P_w \cdot \eta_{\text{GB}} \cdot \eta_{\text{mot}}}{4}, & \text{if } P_w < 0 \end{cases} \tag{1}$$

Moreover, the following balance equation is satisfied under the assumption that the efficiency of the AC-DC and AC-AC converters is unitary: $P_e = 4P_{\text{mot,e}} + P_{\text{aux}} = P_{\text{gen}} + P_{\text{batt}}$, where P_{gen} and P_{batt} are the generator and battery power, respectively, and P_{aux} is the power required by the onboard auxiliary systems.

2.3 Battery Model. The battery pack is composed of $N_S = 124$ cells connected in series and $N_P = 5$ cells connected in parallel (124S5P configuration), with Nickel Manganese Cobalt/Graphite cells modeled through a zero-order equivalent circuit model (ECM). The experimental data in Refs. [24] and [25] are used to obtain the ECM internal resistance $R_{0,\text{cell}}$ and open circuit voltage OCV_{cell} (see Figs. 2 and 3 in Ref. [15]). Since electrical modularity [26] is assumed for all the cells, the cell-level electrical parameters are upscaled to the pack-level through the following equations: $R_{0,\text{batt}} = \frac{N_S}{N_P} \cdot R_{0,\text{cell}}$, $\text{OCV}_{\text{batt}} = N_S \cdot \text{OCV}_{0,\text{cell}}$, $Q_{\text{batt}} = N_P \cdot Q_{\text{cell}}$, where $R_{0,\text{batt}}$, OCV_{batt}, and Q_{batt} are the battery pack internal resistance, open circuit voltage, and capacity, respectively. The battery pack SOC rate, $\dot{\text{SOC}}$, is calculated as follows:

$$\dot{\text{SOC}} = -\frac{I_{\text{batt}}}{Q_{\text{batt}}}, \quad \text{with} \quad I_{\text{batt}} = \frac{\text{OCV}_{\text{batt}} - \sqrt{\text{OCV}_{\text{batt}}^2 - 4R_{0,\text{batt}}P_{\text{batt}}}}{2R_{0,\text{batt}}} \tag{2}$$

where I_{batt} is the battery pack current.

2.4 Electric Generator. The generator power losses are divided into stator copper losses $P_{\text{SCL,gen}}$, rotor copper losses $P_{\text{RCL,gen}}$, iron losses $P_{\text{iron,gen}}$, and friction losses $P_{\text{fric,gen}}$ [27]. Once the power losses are obtained through the induction machine (IM)

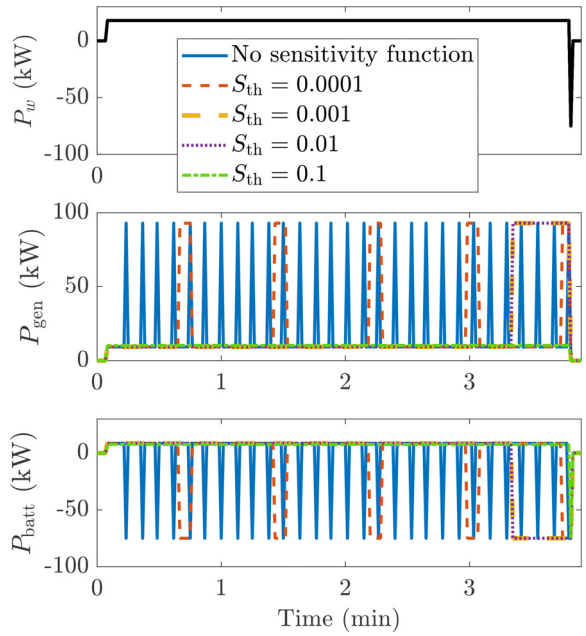

Fig. 2 Power requested at the wheels, generator, and battery power profiles obtained by the ExMS for minimization of thermal emissions over Munson for different S_{th} values

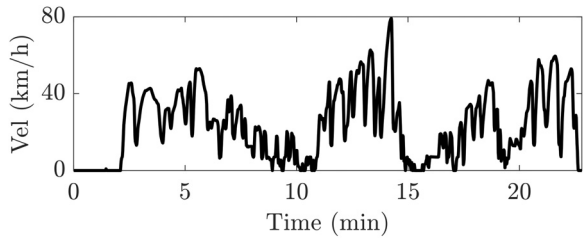

Fig. 3 Velocity, slope, and auxiliary power profiles of the DCE5 driving mission

equivalent circuit model [15], the electric generator efficiency η_{gen} is calculated as follows:

$$\eta_{gen} = \frac{P_{gen}}{P_{gen} + (P_{SCL,gen} + P_{RCL,gen} + P_{iron,gen} + P_{fric,gen})} \tag{3}$$

The generator temperature, T_{gen}, evolves over time according to the following first order thermal dynamics

$$\begin{aligned} C_{gen} \cdot \dot{T}_{gen} &= \dot{Q}_{heat,gen} + P_{SCL,gen} + P_{RCL,gen} + P_{iron,gen} + P_{fric,gen} \\ \dot{Q}_{heat,gen} &= h_{out,gen}(T_0 - T_{gen}) \end{aligned} \tag{4}$$

where $\dot{Q}_{heat,gen}$ is the heat exchange between the generator and the environment, and $h_{out,gen}$ is the relative convective heat transfer coefficient.

The exergy destruction, $\dot{X}_{dest,gen}$, the exergy transfer due to heat exchange between the generator and the environment, $\dot{X}_{heat,gen}$, and the useful work, $\dot{X}_{work,gen}$, are computed through the following equations from [15]

$$\begin{aligned} \dot{X}_{heat,gen} &= \left(1 - \frac{T_0}{T_{gen}}\right) \cdot \dot{Q}_{heat,gen} \\ \dot{X}_{work,gen} &= -\omega_{gen} \cdot \tau_{gen} \\ \dot{X}_{dest,gen} &= -\frac{T_0 \cdot (P_{SCL,gen} + P_{RCL,gen} + P_{iron,gen} + P_{fric,gen})}{T_{gen}} \end{aligned} \tag{5}$$

The generator exergetic terms are shown as speed-torque maps in Ref. [15].

2.5 Internal Combustion Engine. The ICE instantaneous fuel consumption, $\dot{m}_f$, is quantified through the engine speed-torque (ω_{eng}–τ_{eng}) map shown in Ref. [28]. The engine power, P_{eng}, is a function of generator power and efficiency η_{gen}: $P_{eng} = \frac{P_{gen}}{\eta_{gen}}$.

The exergetic model of the ICE from Ref. [28] is used to map each ICE exergy rate term as a function of ω_{eng} and τ_{eng}. The exergy destruction rate $\dot{X}_{dest,eng}$ accounts for the combustion irreversibilities $\dot{X}_{comb,eng}$, the mechanical losses related to friction $\dot{X}_{fric,eng}$, and the exergy destruction of unmodeled phenomena $\dot{X}_{others,eng}$: $\dot{X}_{dest,eng} = \dot{X}_{comb,eng} + \dot{X}_{fric,eng} + \dot{X}_{others,eng}$. While the exergy terms $\dot{X}_{heat,eng}$ and $\dot{X}_{exh,eng}$ quantify the output exergy transfer due to the heat exchange between in-cylinder mixture and cylinder's walls and due to the exhaust gases, respectively, the fuel exergy $\dot{X}_{fuel,eng}$, and the intake air exergy flow $\dot{X}_{intk,eng}$ are the input exergy transfer terms.

2.6 Genset. The strategies proposed in this work aim at minimizing genset exergy destruction and exergy transfer due to heat exchange between the genset and the environment. The exergy destruction of the genset is expressed as the sum of the exergy destruction of ICE and generator

$$\dot{X}_{dest,genset} = \dot{X}_{dest,eng} + \dot{X}_{dest,gen} \tag{6}$$

Since the powertrain component operating at the highest temperature is the one that can be detected more easily by thermal imaging, the $\text{ExMS}_{thermal}$ aims to minimize the exergy transfer due to heat exchange between generator and environment, and ICE and environment. Hence, the genset exergy transfer due to heat exchange is defined as follows:

$$\dot{X}_{heat,genset} = \min(\dot{X}_{heat,eng}(t, P_{batt}, T_{gen}), \dot{X}_{heat,gen}(t, P_{batt}, T_{gen})) \tag{7}$$

based on the formulation in Ref. [15].

3 Optimal Control Problems

The exergy-based strategies are formulated as constrained finite-time optimal control problems to achieve the optimal power-split between the powertrain power sources over a selected driving mission

$$\begin{aligned} P^*_{batt} = \underset{P_{batt}}{\text{argmin}} & \int_{t_0}^{t_f} c_r\big(\text{SOC}(t), P_{batt}(t), P_{mot,e}(t)\big)dt \\ \text{subject to} \quad & \text{SOC}_{target} - \varepsilon \le \text{SOC}(t_f) \le \text{SOC}_{target} + \varepsilon \\ & I_{batt,min} \le I_{batt}(t) \le I_{batt,max} \\ & P_{batt,min} \le P_{batt}(t) \le P_{batt,max} \\ & P_{gen,min} \le P_{gen}(t) \le P_{gen,max} \\ & P_{eng,min} \le P_{eng}(t) \le P_{eng,max} \\ & \text{SOC}_{min} \le \text{SOC}(t) \le \text{SOC}_{max} \\ & \dot{\text{SOC}}(t) = -\frac{I_{batt}(t)}{Q_{batt}} \end{aligned} \tag{8}$$

where t_0 and t_f are the initial and final time instants of the driving mission, c_r is a running cost (that is specified later), P_{batt} is the control variable, SOC is the state variable, and P_e is the exogenous input of the optimal control problem. A global constraint on the final SOC is imposed to reach the SOC_{target} at the end of the mission, within a tolerance ε. Moreover, local constraints are imposed to guarantee the components physical operation limits, such as the minimum $P_{gen,min}$, and maximum $P_{gen,max}$ generator power, the minimum $P_{eng,min}$ and maximum $P_{eng,max}$ engine power, the minimum $P_{batt,min}$ and maximum $P_{batt,max}$ battery power, and

Table 1 Summary of the strategies

Strategy	Optimality of the solution	SOC_{target}	Penalty function	Equivalence factor
Charge sustaining				
ECMS	If the equivalence factor is optimally tuned, the solution is optimal	$SOC(t_0)$	w_{CS}: penalty to satisfy state constraints	Offline calibration
$ExMS_{dest}$				
$ExMS_{thermal}$				
A-ECMS	Suboptimal solution: higher objective function than optimal solution	$SOC(t_0)$	w_{CS}: penalty to satisfy state constraints	Online adaptation
$A\text{-}ExMS_{dest}$				
$A\text{-}ExMS_{thermal}$				
Charge increasing				
ECMS (NP)	Suboptimal solution: final SOC not reached	$SOC_{max} - \varepsilon_{CI}$	No penalty	Offline calibration
$ExMS_{dest}$ (NP)				
$ExMS_{thermal}$ (NP)	Almost identical to optimal DP solution			
ECMS (P)	Close to optimal solution: final SOC reached	$SOC_{max} - \varepsilon_{CI}$	w_{CI}: penalty to reach final desired SOC	Offline calibration
$ExMS_{dest}$ (P)				
$ExMS_{thermal}$ (P)	Almost identical to optimal DP solution			
A-ECMS	Suboptimal solution: higher objective function than optimal solution	$SOC_{max} - \varepsilon_{CI}$	No penalty	Online adaptation
$A\text{-}ExMS_{dest}$				
$A\text{-}ExMS_{thermal}$				

Note that (NP) and (P) refer to the CI ExMSs without and with w_{CI} penalty, respectively.

the minimum $I_{batt,min}$ and maximum $I_{batt,max}$ battery currents. Moreover, the state variable must be maintained in the SOC operating range $[SOC_{min}, SOC_{max}]$ throughout the driving mission.

The strategies proposed in this work are summarized in Table 1. These are categorized based on three criteria. First, they are differentiated based on the final (or target) SOC, i.e., charge sustaining versus charge increasing strategies. The second differentiation is between offline and online strategies. Finally, the strategies are differentiated based on the objective function they minimize, i.e., fuel consumption, exergy destruction, or exergy transfer due to heat exchange.

While the ECMS and A-ECMS minimize the fuel consumption, the $ExMS_{dest}$ and $A\text{-}ExMS_{dest}$ are designed to minimize exergy destruction. Finally, the $ExMS_{thermal}$ and $A\text{-}ExMS_{thermal}$ target the minimization of thermal emissions. Relying on the exergy-based strategies formulation developed in Ref. [15], the running costs used for the strategies proposed in this work are reported in Table 2.

4 Offline Exergy Minimization Strategies

Similar to the ECMS, the ExMS converts the global optimization problem to an instantaneous minimization problem, suitable for online control. In this work, the standard ECMS, the ExMS for the minimization of exergy destruction, and ExMS for the minimization of thermal emissions are formulated to minimize, at each time-step, the respective Hamiltonian function.

Relying on the PMP formulation, the Hamiltonian function H for the problem defined in Sec. 3 is written as follows:

Table 2 Running costs for the different control strategies [15]

Strategy	Running cost c_r
ECMS, A-ECMS	$\dot{m}_f$
$ExMS_{dest}$, $A\text{-}ExMS_{dest}$	$\dot{X}_{dest,genset}$
$ExMS_{thermal}$, $A\text{-}ExMS_{thermal}$	$\dot{X}_{heat,genset}$

$$H(SOC(t), P_{batt}(t), t) = c_r(SOC(t), P_{batt}(t), t) + (\lambda(t) + w_{CS/CI}(t)) \cdot \dot{SOC}(SOC(t), \times P_{batt}(t), t) \quad (9)$$

where λ is the equivalence factor, and w_{CS} and w_{CI} are the additive penalty functions for the charge sustaining and charge increasing strategies, respectively (refer to the following subsections for their formulation). As reported in Table 2, c_r corresponds to the $\dot{m}_f$, $\dot{X}_{dest,genset}$, and $\dot{X}_{heat,genset}$ for the ECMS, $ExMS_{dest}$, and $ExMS_{thermal}$, respectively. For the offline ExMSs, the equivalence factor λ is selected to minimize the cost over a specific driving mission, while satisfying the final SOC constraint. Hence, the bisection algorithm is applied offline to select the appropriate value of the constant λ through the iterative process described in Ref. [14].

4.1 Charge Sustaining Exergy Minimization Strategies and Charge Increasing Exergy Minimization Strategies. The charge sustaining and charge increasing ExMS are developed to meet two different vehicle application requirements, i.e., regular driving, and driving followed by a silent watch mission, respectively. These are achieved by setting different values for the final SOC target.

4.1.1 Charge Sustaining Exergy Minimization Strategies. The charge sustaining ExMS aims to obtain a final SOC equal to the initial SOC

$$SOC_{target} = SOC(t_0) \quad (10)$$

This CS ExMS is appropriate for standard HEV applications where the goal is to obtain the most energetically/exergetically efficient solution, without depleting the battery.

For the CS ECMS and CS ExMS, the additive CS penalty function, w_{CS}, is used to guarantee that the SOC is maintained within the operating range $[SOC_{max}, SOC_{min}]$

$$w_{CS}(SOC) = \begin{cases} 0, & \text{if } SOC_{min} \le SOC(t) \le SOC_{max} \\ -K, & \text{if } SOC(t) > SOC_{max} \\ +K, & \text{if } SOC(t) < SOC_{min} \end{cases} \quad (11)$$

where K is a tuning parameter [14].

4.1.2 Charge Increasing Exergy Minimization Strategies and Equivalent Consumption Minimization Strategy. The charge increasing ExMS is designed for specific military applications in which the driving mission is followed by a silent watch. Its purpose is to charge the battery to a high SOC to provide maximum energy availability before the silent watch

$$SOC_{target} = SOC_{max} - \varepsilon_{CI} \quad (12)$$

where the tolerance ε_{CI} is introduced to prevent exceeding the SOC upper limit.

A newly proposed additive penalty function, w_{CI}, is implemented to guarantee the final SOC target is met. The new additive penalty function w_{CI} for CI ExMS is formulated as a proportional-integral (PI) controller to maintain the SOC near the SOC_{target}

$$w_{CI}(SOC) = \begin{cases} c_P(SOC_{target} - SOC(t)) + c_I \int_{t_0}^{t} (SOC_{target} - SOC(t)), \\ \quad \text{if } 0 < P_e \le P_{e,th} \quad \text{and} \quad SOC_{target} - \varepsilon \le SOC \le SOC_{max} \\ 0, \\ \quad \text{if } P_e < 0 \quad \text{or} \quad P_e > P_{e,th} \quad \text{or} \quad SOC \le SOC_{target} - \varepsilon \end{cases} \quad (13)$$

where c_P and c_I are the proportional and integral gains of the penalty function, and $P_{e,th}$ is an electric power threshold. The additive penalty function is formulated to be active (different from zero) in the last portion of the driving mission when the power requested P_e is positive and lower than the threshold $P_{e,th}$. $P_{e,th}$ is a tuning parameter that must be selected greater than the P_e value toward the end of the mission. The additional activation condition on the SOC ($SOC_{target} - \varepsilon \le SOC \le SOC_{max}$) leads to the activation of the penalty only when the SOC has already reached a value near the maximum. The penalty function w_{CI} proves to be necessary for the ECMS and $ExMS_{dest}$: when tested on the driving scenario presented in Sec. 6, both strategies without the penalty function w_{CI} cannot satisfy the final SOC constraint due to battery discharging in the last portion of the driving mission.

5 Adaptive Exergy Minimization Strategies

The selection of the optimal equivalence factor is a significant hurdle for the online implementation of the ExMS due to lack of knowledge of the driving mission. If a suboptimal equivalence factor value is selected, the ExMS leads to a suboptimal solution and does not guarantee the constraints on the final SOC. Hence, the A-ExMS is introduced to update the equivalence factor during the driving mission so that an initial suboptimal guess of the equivalence factor is corrected online.

In this work, the adaptation method proposed in Ref. [29] for A-ECMS is extended to the formulation of the A-ExMSs. This approach aims to maintain the SOC value near the SOC_{target} by counteracting the SOC deviations. At each time-step, a PI controller takes as input the actual SOC value, $SOC(t)$, and updates the equivalence factor, $\lambda(t)$, to regulate the SOC to the SOC_{target}

$$\lambda(t) = \lambda(t_0) + c_P^A(SOC_{target} - SOC(t)) + c_I^A \int_{t_0}^{t} (SOC_{target} - SOC(t))dt \quad (14)$$

where $\lambda(t_0)$ is the initial λ value; c_P^A and c_I^A are the proportional and integral gains, respectively. If the $SOC(t)$ is higher than SOC_{target}, λ is decreased to encourage battery discharging; on the contrary, if the $SOC(t)$ is lower than SOC_{target}, λ is raised to encourage battery charging. As for any PI controller, the proportional and integral gains must be tuned in order to ensure convergence of the SOC to the SOC_{target} value, avoiding, at the same time, an unstable behavior of the solution. Moreover, also the selection of the initial $\lambda(t_0)$ value influences the solution.

Charge sustaining and CI A-ExMSs are designed to achieve different final SOC values. The SOC_{target} for the CS ExMS can be expressed as in the Eq. (10). The equivalence factor is updated at each time-step through Eq. (14). The CI A-ExMS is formulated under the realistic assumption that although we are aware of an upcoming silent watch, the exact moment the silent watch will begin is not known. Hence, over the mission, the battery is charged to reach the SOC_{target} as fast as possible in anticipation of an upcoming silent watch phase (the constant SOC_{target} is expressed as in Eq. (12)). It is worth noting that before reaching the SOC_{target}, the equivalence factor is kept constant $\lambda = \lambda(t_0)$, and the control variable is selected to charge the battery as much as possible. Once the SOC reaches the SOC_{target} for the first time, it is then maintained near the SOC_{target} by updating the equivalence factor through Eq. (14) for the remaining portion of the mission.

In general, an optimal control policy, whether aimed to minimize fuel consumption or exergy losses, is not designed to ensure drivability constraints [30], thus potentially causing powertrain noise, vibration, and harshness [31]. Previous studies have proposed methods to address the drivability issues for the standard ECMS [31,32].

In this work, the sensitivity function approach proposed in Ref. [30] is adopted to modify the ECMS, ExMS, and A-ExMS solutions to tackle undesired high-frequency component in the ICE power request. At each time-step Δt, the ECMS, ExMS or A-ExMS selects the control variable $P_{batt}(t)$ to minimize the Hamiltonian $H(t)$, and the sensitivity function is calculated as

$$S(t) = \left| \frac{H(t) - H(t - \Delta t)}{P_{gen}(t) - P_{gen}(t - \Delta t)} \right| \quad (15)$$

If the sensitivity function is higher than a given sensitivity function threshold S_{th}, the selected control variable is implemented at time t; otherwise, if the sensitivity function is lower than S_{th}, the selected control is discarded and a suboptimal P_{batt} candidate[1] is implemented. Careful consideration must be paid to the selection of the sensitivity threshold S_{th}, in order to avoid chattering behavior. Once an appropriate S_{th} value is selected, the sensitivity function discards those control candidates which lead to low variations in the cost function, or high variations in the generator power between consecutive time steps, avoiding the undesired chattering behavior.

[1]The sub-optimal candidate is selected as the battery power that minimizes the cost function between the ones that lead to a sensitivity function lower than the threshold.

Table 3 Sensitivity function analysis

	$\text{ExMS}_{\text{thermal}}$				
S_{th}	0.0001	0.001	0.01	0.1	DP
$X_{\text{heat,genset}}$ (kJ)	742.01 (+0.28%)	743.02 (+0.43%)	743.04 (+0.43%)	616.29 (−16.7%)	739.83 (0.0%)
$\text{SOC}(t_f)$	49.63%	49.61%	49.61%	46.56%	49.50%

In Sec. 6, a sensitivity analysis is conducted to find the appropriate sensitivity threshold value.

6 Results

The offline ExMSs are solved for the military vehicle model described in Sec. 2. The results obtained by the ECMS, ExMSs, and A-ExMSs are compared with the respective optimal DP solutions. In the remainder of the paper, the symbols DP_{fc}, DP_{dest}, and $\text{DP}_{\text{thermal}}$ are used to indicate the solution obtained by DP to the ECMS, $\text{ExMS}_{\text{dest}}$, and $\text{ExMS}_{\text{thermal}}$ optimal control problems, respectively. It is worth noting that the SOC_{min} and SOC_{max} are set to 40% and 80%, respectively, for all the simulations.

6.1 Sensitivity Analysis. The ECMS and ExMSs are tested over the Munson driving mission to assess the presence of chattering behavior. Since the Munson is characterized by a constant velocity profile [15], the power requested at the wheels P_w is constant for almost the whole driving mission and the presence of chattering behavior of the generator power is regarded as an indicator of numerical instabilities.

An undesired chattering behavior is observed while testing the ExMS for minimization of thermal emissions over the Munson mission. A sensitivity analysis is carried out to select the appropriate S_{th} value, analyzing the solutions obtained by the ExMS with different values of S_{th}: 0.0001, 0.001, 0.01, 0.1. To evaluate the ExMS solution for each S_{th}, both the reduction of chattering behavior and performance are assessed. The performance is quantified by comparing the exergy losses to the one obtained through DP and assessing the final SOC at the end of the mission, which are reported in Table 3 for each value of S_{th}. On the other hand, the chattering behavior is assessed through the analysis of the power profiles obtained by the ExMS with different values of the sensitivity threshold, shown in Fig. 2. The increase of the S_{th} value leads to lower chattering behavior but slightly lower performance. Based on the obtained results, $S_{\text{th}} = 0.001$ is selected as a good compromise between chattering avoidance and good performance and is adopted in the following simulations.

6.2 Charge Sustaining Exergy Minimization Strategies. The realistic military driving mission DCE5 [33] is used to solve the proposed strategies. The DCE5 is characterized by a variable velocity profile shown in Fig. 3; the slope and auxiliary power are equal to zero for the whole mission.

While the equivalence factor is calibrated offline through the bisection algorithm for the offline ECMS and ExMSs, the A-ECMS and A-ExMSs update the equivalence factor online at each time-step. To test the adaptation ability of the A-ECMS and A-ExMSs, a suboptimal initial value of the equivalence factor $\lambda(t_0)$ is selected for each strategy. The optimal values λ_{opt} of the equivalence factors calibrated offline and the $\lambda(t_0)$ values for the adaptive strategies are reported in Table 4, respectively.

The proportional and integral gains are parameters of the A-ExMS that need to be properly calibrated to obtain an objective function value J close to the DP optimal one J^*, while operating in charge sustaining ($-1\% \leq \Delta\text{SOC} \leq 1\%$, with $\Delta\text{SOC} = \text{SOC}(t_f) - \text{SOC}(t_0)$). For each strategy (A-ECMS, $\text{A-ExMS}_{\text{dest}}$, and $\text{A-ExMS}_{\text{thermal}}$), the solution is obtained over the first 10 min of the DCE5 mission for different values of c_P^A and c_I^A; the results in terms of ΔSOC and $\frac{J}{J^*}$ are reported in Tables 5–7. Based on the presented results, the c_P^A and c_I^A values are selected for each strategy, as highlighted in bold within the Tables: $c_P^A = 32$ and $c_I^A = 0.2$ for the A-ECMS, $c_P^A = 2.5$ and $c_I^A = 0.07$ for the $\text{A-ExMS}_{\text{dest}}$, and $c_P^A = 1$ and $c_I^A = 0.0075$ for the $\text{A-ExMS}_{\text{thermal}}$.

Once the tuning parameters are selected, the proposed strategies are tested over the whole DCE5 mission. In Fig. 4, the generator, battery, and braking power selected by the different management strategies are depicted as functions of the power requested at the

Table 4 Optimal equivalence factor and initial equivalence factor for the adaptive strategies

	A-ECMS	$\text{A-ExMS}_{\text{dest}}$	$\text{A-ExMS}_{\text{thermal}}$
λ_{opt}	2.21	0.77	5.60×10^{-2}
$\lambda(t_0)$	3	1	0.1

The bold values indicate the selected gains

Table 5 SOC deviation from the $\text{SOC}_{\text{target}}$ and $\frac{m_f}{m_f^*}$ obtained by the A-ECMS for different values of c_P^A and c_I^A over the first 10 min of DCE5

		c_P^A						c_P^A			
$\Delta\text{SOC}(\%)$		16	32	64	128	$\frac{\dot{m}_f}{\dot{m}_f^*}$		16	32	64	128
c_I^A	0.05	0.45	0.9	1.08	1.01	c_I^A	0.05	1.02	1.02	1.02	1.02
	0.1	0.7	0.56	0.76	0.83		0.1	1.02	1.01	1.02	1.02
	0.2	0.67	**0.60**	0.58	0.65		0.2	1.02	**1.01**	1.01	1.02
	0.4	1.12	0.71	0.56	0.56		0.4	1.02	1.02	1.02	1.02

The bold values indicate the selected gains

Table 6 SOC deviation from the $\text{SOC}_{\text{target}}$ and $\frac{\dot{X}_{\text{dest,genset}}}{\dot{X}^*_{\text{dest,genset}}}$ obtained by the $\text{A-ExMS}_{\text{dest}}$ for different values of c_P^A and c_I^A over the first 10 min of DCE5

		c_P^A						c_P^A			
ΔSOC		1.25	2.5	5	10	$\frac{\dot{X}_{\text{dest,genset}}}{\dot{X}^*_{\text{dest,genset}}}$		1.25	2.5	5	10
c_I^A	0.0175	0.33	0.08	0.35	0.72	c_I^A	0.0175	1.02	1.01	1.01	1.01
	0.035	2.99	1.47	0.6	0.5		0.035	1.04	1.02	1.01	1.01
	0.075	0.75	**0.8**	0.72	0.54		0.075	1.02	**1.01**	1.01	1.01
	0.15	2.1	1.88	1.15	0.65		0.15	1.03	1.03	1.02	1.01

The bold values indicate the selected gains

Table 7 SOC deviation from the $\text{SOC}_{\text{target}}$ and $\frac{\dot{X}_{\text{heat,genset}}}{\dot{X}^*_{\text{heat,genset}}}$ obtained by the $\text{A-ExMS}_{\text{thermal}}$ for different values of c_P^A and c_I^A over the first 10 min of DCE5

		c_P^A						c_P^A			
ΔSOC		0.25	0.5	1	2	$\frac{\dot{X}_{\text{heat,genset}}}{\dot{X}^*_{\text{heat,genset}}}$		0.25	0.5	1	2
c_I^A	0.0015	−2.46	−1.39	−0.05	0.84	c_I^A	0.0015	1.02	1.01	1.01	1.02
	0.0035	1.47	−1.04	−0.41	0.22		0.0035	1.04	1.01	1.01	1.02
	0.0075	−1.38	−0.70	**−0.38**	0.08		0.0075	1.02	1.01	**1.01**	1.02
	0.015	1.31	0.06	−0.16	0.01		0.015	1.02	1.02	1.01	1.02

The bold values indicate the selected gains

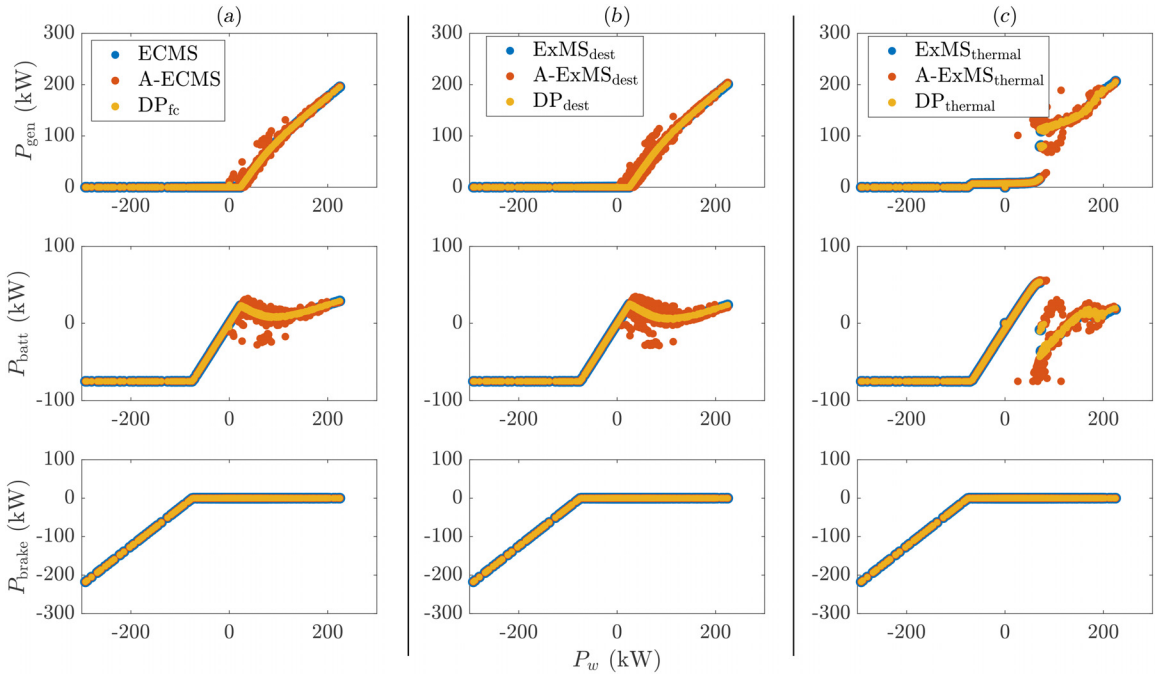

Fig. 4 Generator, battery and mechanical brake power profiles as a function of power requested at the wheels for all the charge sustaining strategies over the DCE5 mission. Column (*a*) shows the energy-based strategies, column (*b*) the exergy-based strategies for minimization of exergy destruction, and column (*c*) the exergy-based strategies for minimization of thermal emissions.

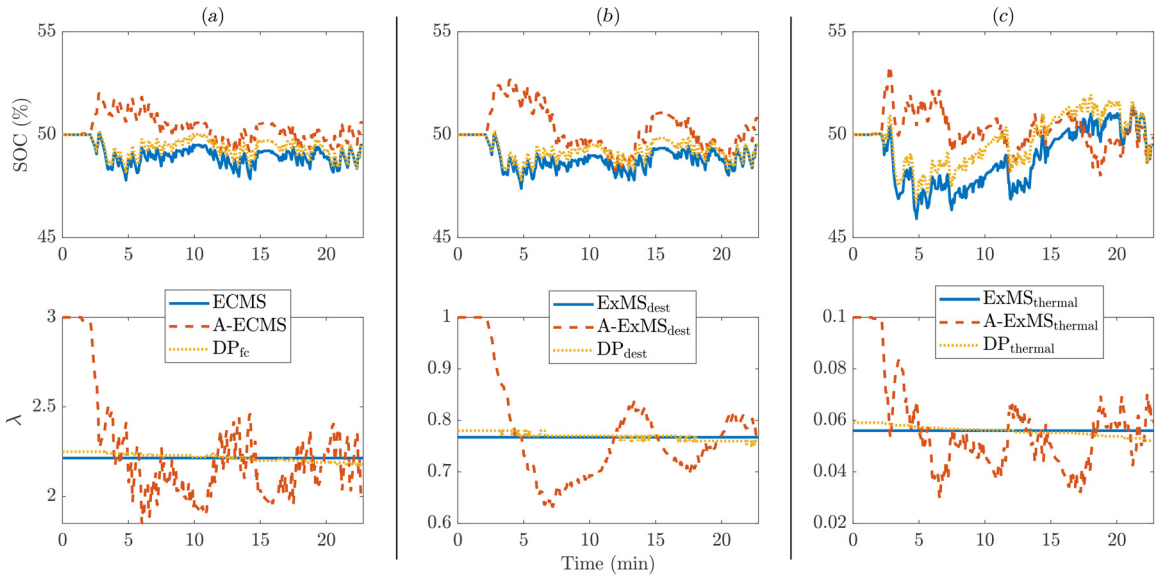

Fig. 5 SOC and equivalence factor profiles obtained by all the charge sustaining strategies over the DCE5 mission. Column (*a*) shows the energy-based strategies, column (*b*) the exergy-based strategies for minimization of exergy destruction, and column (*c*) the exergy-based strategies for minimization of thermal emissions.

wheels. Analyzing the energy-based strategies results in the first column of Fig. 4, it is possible to note that the power-split obtained by DP$_{fc}$ and ECMS are almost identical, while some differences are present in the A-ECMS power profiles. These differences are caused by the different equivalence factor profiles, shown in the lower subplot of Fig. 5. Since the initial λ value is higher than λ_{opt}, the battery is charged at the beginning of the mission by the A-ECMS, while the other algorithms tend to discharge the battery. As a consequence, the SOC profile obtained by the A-ECMS is visibly different compared to the other algorithms. A small difference is also present between the ECMS and DP$_{fc}$ SOC profiles. Although ECMS leads to a quasi-optimal solution, the equivalence factor should vary during the mission to obtain a solution identical to DP$_{fc}$, based on the PMP theory [14]. Indeed, the fictitious equivalence factor for DP$_{fc}$ varies over time with a slightly decreasing trend. The DP$_{fc}$ fictitious λ values correspond to the λ values that should be used in the ECMS in order to select the same P_{batt} selected by DP over the mission.

The ExMS$_{dest}$ and A-ExMS$_{dest}$ lead to a similar power-split to the one obtained with ECMS and A-ECMS, respectively. The similarities between the control policy of the exergy-based strategies for minimization of exergy destruction and

energy-based strategies can be explained by the fact that those exergy-based strategies aim to minimize the irreversibilities, which is comparable to the energy-based strategies implicit minimization of system inefficiencies to reduce fuel consumption. Also in this case, due to the higher initial equivalence factor, the battery is charged at the beginning by the A-ExMS$_{dest}$, while the ExMS$_{dest}$ and DP$_{dest}$ tend to discharge the battery. Afterward, the ExMS$_{dest}$ equivalence factor is correctly updated and progressively converges to the optimal ExMS$_{dest}$ one, as shown in the second column of Fig. 5. As a consequence, the SOC profiles display different trends at the beginning, overlapping in later phases of the mission. The slight difference between SOC profiles obtained by ExMS$_{dest}$ and DP$_{dest}$ are once again explained by the suboptimality of the constant equivalence factor for the ExMS$_{dest}$.

The exergy-based strategies for minimization of thermal emissions lead to very different power-splits compared to the other strategies. As shown in the third column of Fig. 4, the battery power P_{batt} selected by thermal emissions abruptly changes when the power requested at the wheels is about 80 kW. Indeed, all three ExMS$_{thermal}$, A-ExMS$_{thermal}$, and DP$_{thermal}$ select specific generator powers between 7 and 15 kW, and over 100 kW in order to minimize the exergy transfer due to heat exchange. The high P_{gen} are selected to operate the ICE at high speed, reducing the in-cylinder gas temperature and the heat transfer between the ICE and the environment [15].

Fuel consumption, genset exergy destruction, and genset exergy transfer due to heat exchange are quantified in Fig. 6 to compare the performance of the different control algorithms over the DCE5 mission. The solutions obtained through DP$_{dest}$ and ExMS$_{dest}$ are comparable to those obtained by the DP$_{fc}$ and standard ECMS, achieving at most 0.3% more fuel consumption and 1.1% less exergy destruction than standard DP$_{fc}$. On the other hand, the ExMS$_{thermal}$ for minimization of thermal emissions and DP$_{thermal}$ achieve significant reduction (over 30%) of thermal emissions proving to be a suitable approach to avoid thermal imaging detection in military applications, but producing at least 19% higher fuel consumption and 28% higher exergy destruction than the energy-based strategies. The adaptive ECMS and ExMSs achieve slightly suboptimal solutions, reaching around 2% higher objective function than the respective optimal DP solutions.

6.3 Charge Increasing Exergy Minimization Strategies. The CI ExMSs and A-ExMSs are tested over the DS driving scenario composed of two different military driving missions (A and B) and two silent watch phases. The velocity, slope and auxiliary power profiles required during the driving scenario are shown in Fig. 7. The driving missions are characterized by varying velocity and slope

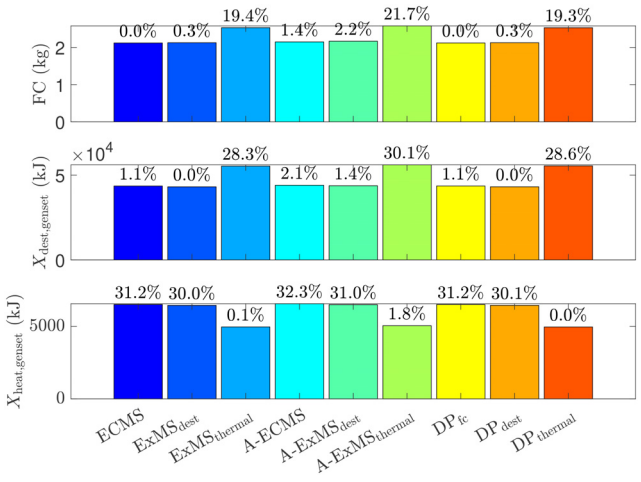

Fig. 6 Cumulative fuel consumption, genset exergy destruction, and genset exergy transfer due to heat exchange obtained by charge sustaining ECMS, ExMSs, and DP

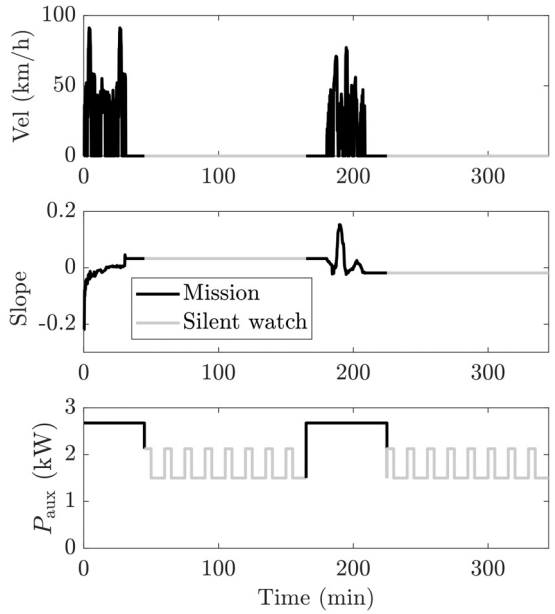

Fig. 7 Velocity, slope, and auxiliary power profiles of the DS scenario, characterized by the two driving missions A and B, each followed by a silent watch

profiles, while the $P_{aux} = 2.6$ kW is constant for both missions. During the silent watch, the vehicle velocity is equal to zero, and the electric power requested by the auxiliaries oscillates between 2.125 kW and 1.5 kW. In this scenario, two optimal control problems are solved, one for each driving mission. The initial SOC for the second control problem (mission B) corresponds to the SOC obtained at the end of the first silent watch. Moreover, it is worth specifying that the final desired SOC (SOC$_{target}$ = 80%) has to be reached at the end of each mission.

For the CI A-ECMS and A-ExMSs, the proportional and integral gains are calibrated over the driving mission A of the DS scenario, to obtain an objective function value J close to the DP one, i.e., J^*, and charge the battery as much as possible, reaching an final SOC equal or greater than SOC$_{target}$ at the end of the mission ($\Delta SOC \geq 0$, with $\Delta SOC = SOC(t_f) - SOC_{target}$). For each strategy, the solution is obtained for different values of c_P^A and c_I^A, with the same initial equivalence factor. The ΔSOC and the $\frac{J}{J^*}$ obtained for every combination of c_P^A and c_I^A by the CI A-ECMS, A-ExMS$_{dest}$, and A-ExMS$_{thermal}$ are reported in Tables 8–10, respectively. Based on the presented results, the c_P^A and c_I^A values are selected for each strategy, as highlighted in bold within the Tables: $c_P^A = 64$ and $c_I^A = 0.8$ for the A-ECMS, $c_P^A = 20$ and $c_I^A = 0.5$ for the A-ExMS$_{dest}$, and $c_P^A = 1$ and $c_I^A = 0.035$ for the A-ExMS$_{thermal}$. After the calibration process, the tuned A-ECMS, and A-ExMSs are tested over the whole DS driving scenario (not just the mission A used for calibration of c_P and c_I). Since mission B of the DS driving scenario is different from mission A, the adaptive strategies are hence tested on different driving conditions from the tuning ones.

Table 8 SOC deviation from the SOC$_{target}$ and $\frac{m_f}{m_f^*}$ obtained by the A-ECMS for different values of c_P^A and c_I^A over the mission A of the DS scenario

		c_P^A						c_P^A			
ΔSOC		16	32	64	128	$\frac{\dot{m}_f}{\dot{m}_f^*}$		16	32	64	128
c_I^A	0.4	0	0	−0.03	−0.015	c_I^A	0.4	1.16	1.16	1.15	1.15
	0.8	0	0	**0**	−0.02		0.8	1.15	1.15	**1.14**	1.15
	1.6	0	0	0	0		1.6	1.15	1.14	1.14	1.15
	3.2	−0.05	0	0	0		3.2	1.21	1.18	1.15	1.15

The bold values indicate the selected gains

Table 9 SOC deviation from the SOC_{target} and $\frac{\dot{X}_{dest,genset}}{\dot{X}^*_{dest,genset}}$ obtained by the A-$ExMS_{dest}$ for different values of c_P^A and c_I^A over the mission A of the DS scenario

		c_P^A				$\frac{\dot{X}_{dest,genset}}{\dot{X}^*_{dest,genset}}$		c_P^A			
ΔSOC		5	10	20	40			5	10	20	40
c_I^A	0.125	0	0	−0.04	−0.18	c_I^A	0.125	1.12	1.11	1.11	1.11
	0.25	0	0	0	−0.03		0.25	1.11	1.11	1.11	1.11
	0.5	0	0	**0**	0		0.5	1.10	1.11	**1.10**	1.11
	1	−0.1	0	0	0		1	1.15	1.13	1.12	1.11

The bold values indicate the selected gains

Table 10 SOC deviation from the SOC_{target} and $\frac{\dot{X}_{heat,genset}}{\dot{X}^*_{heat,genset}}$ obtained by the A-$ExMS_{thermal}$ for different values of c_P^A and c_I^A over the mission A of the DS scenario

		c_P^A				$\frac{\dot{X}_{heat,genset}}{\dot{X}^*_{heat,genset}}$		c_P^A			
ΔSOC		0.5	1	2	4			0.5	1	2	4
c_I^A	0.0015	1	1	1	1	c_I^A	0.0015	1.18	1.18	1.18	1.18
	0.0035	1	**1**	1	1		0.0035	1.17	**1.17**	1.17	1.18
	0.0075	−0.22	0.20	0.15	0.05		0.0075	1.19	1.19	1.18	1.18
	0.015	−0.97	−0.93	−0.85	−0.7		0.015	1.23	1.21	1.20	1.19

The bold values indicate the selected gains

The results obtained by the offline ECMS and ExMSs with (P) and without (NP) the penalty function formulated in Sec. 4, and by the A-ECMS, and A-ExMSs, are compared to the benchmark DP solution over the DS driving scenario. For the ECMS and $ExMS_{dest}$ with penalty function, the power threshold $P_{e,th} = 3$ kW is selected greater than the electrical power requested toward the end of the mission ($P_e = 2.5$ kW) in order to activate the penalty in the last minutes of the mission. On the other hand, for the $ExMS_{thermal}$, the penalty function does not need to be active since the final SOC constraint is already satisfied without the penalty function and, consequently, $P_{e,th}$ is selected to be equal to 0 kW.

Starting with the energy-based strategies, the power-split obtained by the CI ECMS(NP), ECMS(P), A-ECMS and DP_{fc} over the whole DS are shown as a function of the power requested at the wheels in first column of Fig. 8. For the sake of clarity, a zoom of the power profiles against time over the first mission A of the DS are provided in Fig. 9. ECMS with and without penalty and DP_{fc} lead to similar power-split: the main differences between the control policies are related to a more frequent use of the mechanical brakes by ECMS(NP) and ECMS(P), achieving a slightly less efficient solution than DP_{fc}. Moreover, the use of the penalty function in the ECMS(P) leads to a higher generator power than the ECMS(NP) in the last minutes of each driving mission, avoiding battery discharging and enabling to reach the desired final SOC at the end of each mission. On the other hand, the A-ECMS selects significantly different generator and battery powers compared to the other algorithms. At the beginning of each mission, the battery is charged using the minimum battery power $P_{batt,min}$ to reach the SOC_{target} as quickly as possible. After the SOC_{target} is reached for the first time, A-ECMS selects higher battery powers than the other algorithms to discharge the battery and maintain the SOC near the SOC_{target}. However, since the A-ECMS operates near the SOC_{max} for a long period of time, the mechanical brakes are frequently used to satisfy the constraint on the SOC upper limit ($SOC \leq SOC_{max}$), reducing the vehicle efficiency. SOC profiles in the first column of Fig. 10 show that all the energy-based strategies reach the final desired SOC at the end of each mission, except for the ECMS without penalty function. In the lower subplot of Fig. 10, the equivalence factor profile is shown. The equivalence factor is not represented during the silent watch phases, since the battery is the only active power source, and no power-split control strategy is needed.

Similar considerations can be drawn about the power-split, SOC, and equivalence factor profiles obtained by the CI ExMS and A-ExMS for minimization of exergy destruction. For $ExMS_{dest}$ as well, using the penalty function is essential to satisfy the final SOC constraint at the end of the mission.

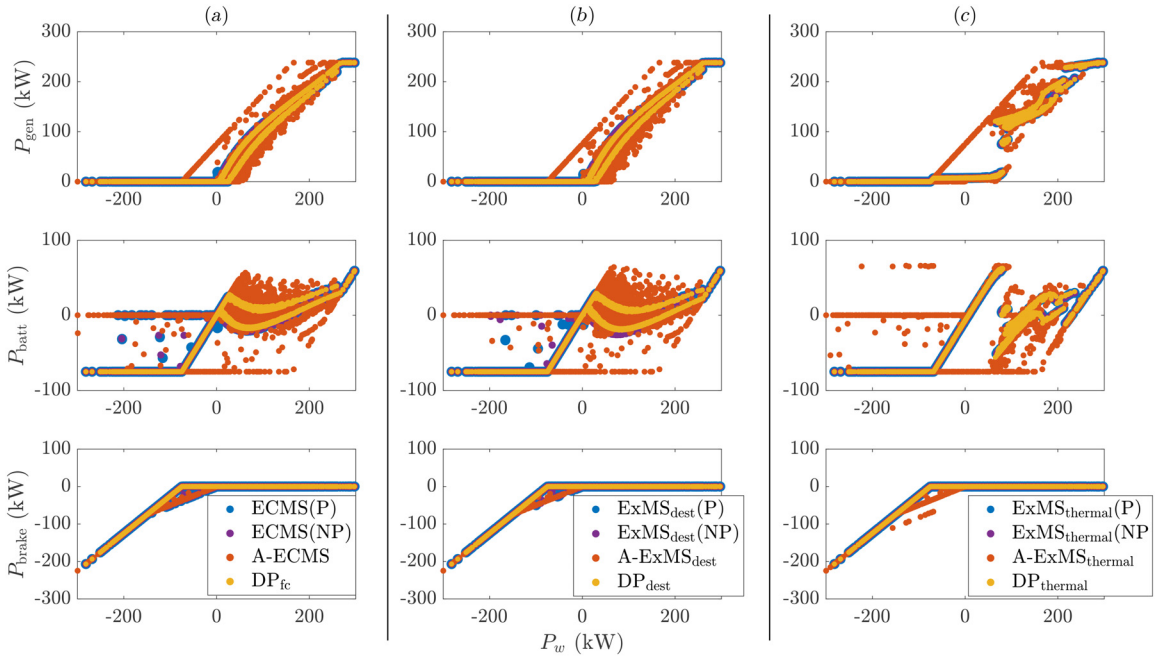

Fig. 8 Generator, battery, and mechanical brake power profiles as a function of power requested at the wheels for all the charge increasing strategies over the DS scenario. Column (*a*) shows the energy-based strategies, column (*b*) the exergy-based strategies for minimization of exergy destruction, and column (*c*) the exergy-based strategies for minimization of thermal emissions.

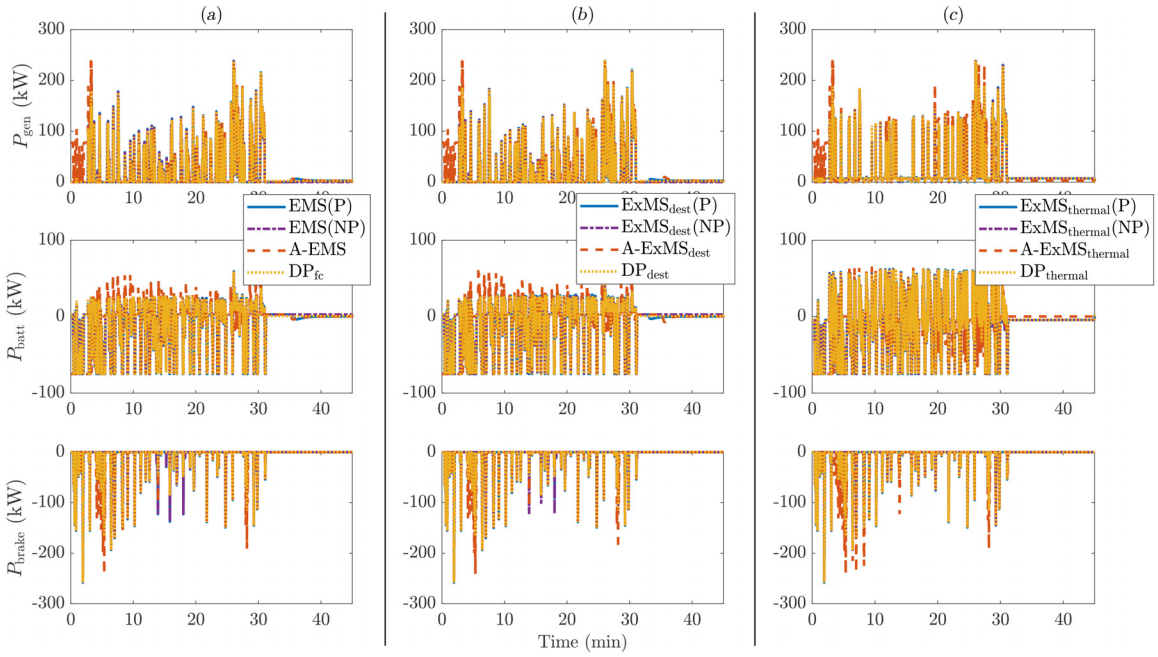

Fig. 9 Generator, battery, and mechanical brake power profiles as a function of time for all the charge increasing strategies over the driving mission A of the DS scenario. Column (*a*) shows the energy-based strategies, column (*b*) the exergy-based strategies for minimization of exergy destruction, and column (*c*) the exergy-based strategies for minimization of thermal emissions.

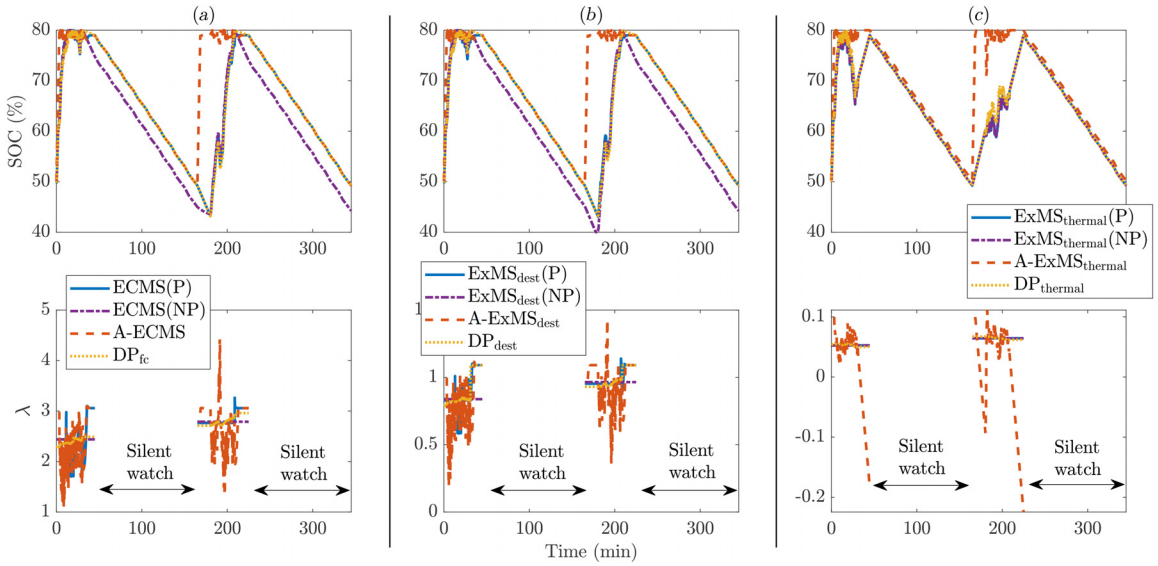

Fig. 10 SOC and equivalence factor profiles obtained by all the charge increasing strategies over the DS scenario. Column (*a*) shows the energy-based strategies, column (*b*) the exergy-based strategies for minimization of exergy destruction, and column (*c*) the exergy-based strategies for minimization of thermal emissions.

Once again, the exergy-based strategies for minimization of thermal emissions obtain significantly different results from the energy-based strategies and exergy-based strategies for minimization of exergy destruction. The use of the penalty function is not necessary for the $ExMS_{thermal}$, since the SOC_{target} is reached at the end of each mission by the $ExMS_{thermal}$ without penalty. This result is explained by the fact that the $ExMS_{thermal}$(NP) selects a generator power higher than zero to minimize the exergy transfer due to heat exchange toward the end of the mission, consequently charging the battery. Therefore, the power threshold for the $ExMS_{thermal}$(P) and $ExMS_{thermal}$(P) is selected to be equal to zero to avoid the activation of the penalty function. The performance obtained by the $ExMS_{thermal}$(P) and $ExMS_{thermal}$(NP) is comparable to the benchmark solution provided by DP, achieving a negligibly higher (0.1%) exergy loss. Even the CI A-$ExMS_{thermal}$ meets the final SOC constraint by reaching the maximum SOC at the end of each mission. The generator power is kept as high as possible in the last portion of the mission to minimize thermal emissions, consequently maintaining the SOC equal to the maximum value.

The cumulative fuel consumption, exergy destruction, and exergy transfer due to heat exchange obtained by all the algorithms over the whole DS driving scenario are reported in Fig. 11. In contrast to the CS ECMS and ExMSs, the CI ECMS and ExMSs obtain suboptimal results compared to the DP benchmark. While the solutions obtained

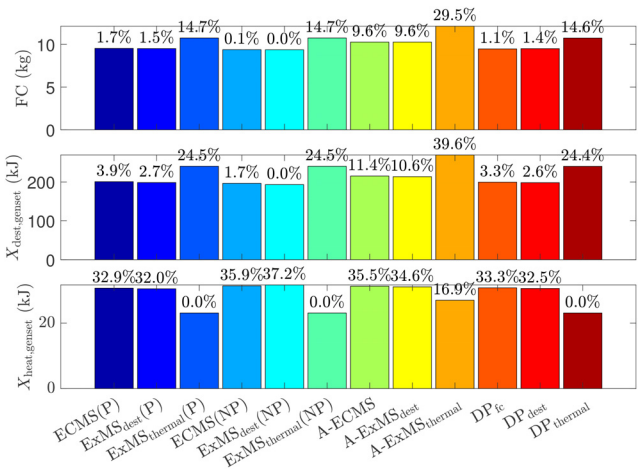

Fig. 11 Cumulative fuel consumption, genset exergy destruction, and genset exergy transfer due to heat exchange obtained by charge increasing ECMS, ExMSs, and DP over the DS scenario

by the ECMS and ExMS$_{dest}$ without penalty achieve lower fuel consumption and exergy loss than DP$_{fc}$ and DP$_{dest}$ because the final SOC constraint is not met, the ECMS and ExMS$_{dest}$ with penalty lead to slightly (around 1%) higher fuel consumption and exergy destruction than DP$_{fc}$ and DP$_{dest}$, respectively. On the other hand, the ExMS$_{thermal}$ with and without penalty achieves almost identical results to DP$_{thermal}$, with only a negligibly higher exergy loss. Due to completely different control policies, the solutions obtained through the adaptive A-ECMS and A-ExMSs differ from the DP optimal results, achieving significantly higher fuel consumption and exergy loss. Since the SOC is maintained close to the SOC upper limit for almost the whole mission, the regenerative braking is often avoided with the consequent decrease in the energetic and exergetic efficiency of the solution.

Finally, to assess the real-time capability of the proposed strategies, the computational time is quantified. Since the computational time is significantly lower than the duration of the driving scenario, the applicability of the ExMS and A-ExMS for online control is demonstrated. The computational time required to solve the strategies over the DCE5 mission and the DS driving scenario with 2 silent watch phases are about 6 and 19 s, respectively. The experiments were run on a computer with an AMD EPYC 7713 64-Core processor running at 2 GHz, with 512 GB of RAM. Given the same vehicle model and the same driving mission, the computational times required to solve the energy-based and exergy-based strategies over the same driving mission are very close.

7 Conclusions

In this work, the exergy minimization strategies for ground HEVs online control are formulated. First, all main components of a series military M-ATV are modeled from the energetic standpoint and the genset exergy model is formulated by relying on the exergetic framework developed in Ref. [11], and adopting the comprehensive ICE exergy model developed in Ref. [28]. Afterward, based on the formulation of the ECMS, the exergy minimization strategies are developed as online strategies to minimize genset exergy destruction and thermal emissions, respectively. While the first ExMS$_{dest}$ aims at the minimization of genset irreversibilities to increase the vehicle efficiency, the second ExMS$_{thermal}$ can be used in military applications to prevent thermal imaging detection from adversary units. Moreover, the A-ExMSs are formulated as online control strategies that adapt the equivalence factor in real-time.

The CS and CI ExMSs are developed to obtain different final SOC at the end of the driving mission. The CS ExMS aims to achieve charge sustainability and enables to obtain the most energetically/exergetically efficient solution, without depleting the battery charge; on the other hand, the CI ExMS is useful for military driving missions followed by a silent watch, recharging the battery as much as possible before the silent watch phase.

The CS and CI ExMSs and A-ExMSs are tested over the DCE5 mission and a complex driving scenario, respectively, and their results are compared to the respective benchmark solutions provided by DP. While the CS ExMSs closely mirror the control policy of the respective DP solutions, the CS A-ExMSs obtains slightly higher exergy loss than DP. Moreover, the proposed penalty function for the CI ECMS and ExMSs allows the battery to be charged as much as possible during the mission, obtaining fuel consumption and exergy loss slightly higher (around 1%) than the respective DP benchmark solutions. For the online application, the A-ECMS and A-ExMSs achieve significantly higher fuel consumption and exergy loss than DP.

Data Availability Statement

The authors attest that all data for this study are included in the paper.

Nomenclature

A = frontal area (m^2)
C = thermal capacity (J/K)
C_r, C_x = roll and drag coefficients
F_{brake} = brake mechanical force (N)
h_{out} = convective coefficient (W/K)
I_{cell} = cell current (A)
J = cost function
LHV = fuel lower heating value (J/kg)
M = vehicle mass (kg)
N_P = number of battery cells connected in parallel
N_S = number of battery cells connected in series
OCV_{cell} = open circuit voltage of a cell (V)
P = power (W)
$P_{fric,gen}$ = friction power loss of generator (W)
$P_{iron,gen}$ = iron power loss of generator (W)
$P_{RCL,gen}$ = rotor copper power loss of generator (W)
$P_{SCL,gen}$ = stator copper power loss of generator (W)
P_w = power required at the wheels (W)
Q_{cell} = capacity of a cell (Ah)
$Q_{heat,cell}$ = convective heat exchanged between cell and environment (J)
$R_{0,cell}$ = internal resistance of a cell (Ω)
SOC = state of charge of the battery
T = temperature (K)
X = exergy (J)
$X_{comb,eng}$ = exergy destruction due to combustion irreversibilities (J)
$X_{exh,eng}$ = exergy transfer of exhaust gas (J)
$X_{fric,eng}$ = exergy destruction due to friction (J)
$X_{fuel,eng}$ = exergy related to fuel (J)
$X_{intk,eng}$ = exergy related to intake air (J)
$X_{others,eng}$ = exergy destruction of unmodeled phenomena (J)
$X_{work,eng}$ = exergy related to work (J)
η = energy efficiency
θ = slope (rad)
λ = equivalence factor
v = vehicle speed (m/s)
ρ_a = air density (kg/m^3)
τ = torque (Nm)
ω = rotating speed (rad/s)

Notation

batt, cell = subscripts for battery pack and battery cell, respectively
dest, heat = subscripts for exergy destruction and heat exchange
eng, gen, mot = subscripts for internal combustion engine, generator, and motor, respectively

$\dot{\chi}$ = time derivative of a variable χ
0 = reference state

References

[1] Tsatsaronis, G., 2007, "Definitions and Nomenclature in Exergy Analysis and Exergoeconomics," Energy, **32**(4), pp. 249–253.
[2] Dincer, I., and Rosen, M. A., 2012, *Exergy: Energy, Environment and Sustainable Development*, Newnes, Oxford, UK.
[3] Moorhouse, D. J., and Camberos, J. A., 2011, *Exergy Analysis and Design Optimization for Aerospace Vehicles and Systems*, American Institute of Aeronautics and Astronautics, Reston, VA.
[4] Naserbegi, A., and Aghaie, M., 2021, "Exergy Optimization of Nuclear-Solar Dual Proposed Power Plant Based on Gwo Algorithm," Prog. Nucl. Energy, **140**, p. 103925.
[5] Kallio, S., and Siroux, M., 2020, "Energy Analysis and Exergy Optimization of Photovoltaic-Thermal Collector," Energies, **13**(19), p. 5106.
[6] Dong, Z., Li, D., Wang, Z., and Sun, M., 2018, "A Review on Exergy Analysis of Aerospace Power Systems," Acta Astronaut., **152**, pp. 486–495.
[7] Evola, G., Costanzo, V., and Marletta, L., 2018, "Exergy Analysis of Energy Systems in Buildings," Buildings, **8**(12), p. 180.
[8] Razmara, M., Maasoumy, M., Shahbakhti, M., and Robinett, R., III, 2015, "Optimal Exergy Control of Building HVAC System," Appl. Energy, **156**, pp. 555–565.
[9] Rakopoulos, C. D., and Giakoumis, E. G., 2006, "Second-Law Analyses Applied to Internal Combustion Engines Operation," Prog. Energy Combust. Sci., **32**(1), pp. 2–47.
[10] Razmara, M., Bidarvatan, M., Shahbakhti, M., and Robinett, R., III, 2016, "Optimal Exergy-Based Control of Internal Combustion Engines," Appl. Energy, **183**, pp. 1389–1403.
[11] Dettù, F., Pozzato, G., Rizzo, D. M., and Onori, S., 2021, "Exergy-Based Modeling Framework for Hybrid and Electric Ground Vehicles," Appl. Energy, **300**, p. 117320.
[12] Kramer, D. M., and Parker, G. G., 2011, "Current State of Military Hybrid Vehicle Development," Int. J. Electr. Hybrid Veh., **3**(4), pp. 369–387.
[13] Mittal, V., Novoselich, B., and Rodriguez, A., 2022, "Hybridization of U.S. Army Combat Vehicles," SAE Paper No. 2022-01-0371.
[14] Onori, S., Serrao, L., and Rizzoni, G., 2016, *Hybrid Electric Vehicles: Energy Management Strategies*, Springer, London, UK.
[15] Acquarone, M., Pozzato, G., James, C., and Onori, S., 2023, "Exergy Management Strategies for Hybrid Electric Ground Vehicles: A Dynamic Programming Solution," ASME J. Dyn. Syst., Meas., Control, **146**(3), p. 031004.
[16] Hofman, T., Steinbuch, M., Van Druten, R., and Serrarens, A., 2007, "Rule-Based Energy Management Strategies for Hybrid Vehicles," Int. J. Electr. Hybrid Veh., **1**(1), pp. 71–94.
[17] Sampathnarayanan, B., Serrao, L., Onori, S., Rizzoni, G., and Yurkovich, S., 2009, "Model Predictive Control as an Energy Management Strategy for Hybrid Electric Vehicles," ASME Paper No. DSCC2009-2671.
[18] Biswas, A., Acquarone, M., Wang, H., Miretti, F., Misul, D. A., and Emadi, A., 2024, "Safe Reinforcement Learning for Energy Management of Electrified Vehicle With Novel Physics-Informed Exploration Strategy," IEEE Trans. Transp. Electrif., **10**(4) p. 1.
[19] Serrao, L., Onori, S., and Rizzoni, G., 2009, "ECMS as a Realization of Pontryagin's Minimum Principle for HEV Control," 2009 American Control Conference, Chicago, IL, June 10–12, pp. 3964–3969.
[20] Onori, S., and Serrao, L., 2011, "On Adaptive-Ecms Strategies for Hybrid Electric Vehicles," 2nd International Scientific Conference on Hybrid and Electric Vehicles RHEVE 2011, Malmaison, France, Dec. 6–7, pp. 1–10.
[21] Mamun, A.-A., Liu, Z., Rizzo, D. M., and Onori, S., 2019, "An Integrated Design and Control Optimization Framework for Hybrid Military Vehicle Using Lithium-Ion Battery and Supercapacitor as Energy Storage Devices," IEEE Trans. Transp. Electrif., **5**(1), pp. 239–251.
[22] Kim, Y., Salvi, A., Siegel, J. B., Filipi, Z. S., Stefanopoulou, A. G., and Ersal, T., 2014, "Hardware-in-the-Loop Validation of a Power Management Strategy for Hybrid Powertrains," Control Eng. Pract., **29**, pp. 277–286.
[23] Mi, C., and Masrur, M. A., 2017, *Hybrid Electric Vehicles: Principles and Applications With Practical Perspectives*, Wiley, Hoboken, NJ.
[24] Catenaro, E., Rizzo, D. M., and Onori, S., 2021, "Experimental Analysis and Analytical Modeling of Enhanced-Ragone Plot," Appl. Energy, **291**, p. 116473.
[25] Catenaro, E., and Onori, S., 2021, "Experimental Data of Lithium-Ion Batteries Under Galvanostatic Discharge Tests at Different Rates and Temperatures of Operation," Data Brief, **35**, p. 106894.
[26] Allam, A., Onori, S., Marelli, S., and Taborelli, C., 2015, "Battery Health Management System for Automotive Applications: A Retroactivity-Based Aging Propagation Study," 2015 American Control Conference (ACC), Chicago, IL, July 1–3, pp. 703–716.
[27] Chapman, S., 2005, *Electric Machinery Fundamentals*, The McGraw-Hill Companies, New York.
[28] Pozzato, G., Rizzo, D. M., and Onori, S., 2022, "Mean-Value Exergy Modeling of Internal Combustion Engines: Characterization of Feasible Operating Regions," ASME J. Dyn. Syst., Meas., Control, **144**(6), p. 061009.
[29] Kessels, J. T., Koot, M. W., Van Den Bosch, P. P., and Kok, D. B., 2008, "Online Energy Management for Hybrid Electric Vehicles," IEEE Trans. Veh. Technol., **57**(6), pp. 3428–3440.
[30] Koprubasi, K., 2008, "Modeling and Control of a Hybrid-Electric Vehicle for Drivability and Fuel Economy Improvements," Ph.D. thesis, The Ohio State University, Columbus, OH.
[31] Arata, J., Leamy, M., and Cunefare, K., 2012, "Power-Split HEV Control Strategy Development With Refined Engine Transients," SAE Int. J. Altern. Powertrains, **1**(1), pp. 119–133.
[32] Skugor, B., Ranogajec, V., and Deur, J., 2013, "On Smoothing HEV/EREV Supervisory Control Action Using an Extended ECMS Approach," 2013 World Electric Vehicle Symposium and Exhibition (EVS27), Barcelona, Spain, Nov. 17–20, pp. 1–10.
[33] Liu, Z., Mamun, A.-A. M., Rizzo, D. M., and Onori, S., 2018, "Combined Battery Design Optimization and Energy Management of a Series Hybrid Military Truck," SAE Int. J. Altern. Powertrains, **7**(2), pp. 155–168.